STUDY OF A WINTER MONSOON FRONT OVER THE SOUTH CHINA SEA BY MULTI- SENSOR SATELLITE AND WEATHER RADAR DATA, AND A NUMERICAL MODEL

Werner Alpers (1), Wai Kin Wong (2), Knut-Frode Dagestad (3), Pak Wai Chan (2)

(1) Centre for Marine and Atmospheric Sciences (ZMAW), Institute of Oceanography, University of Hamburg, Bundesstrasse 53, 20146 Hamburg, Germany, Email: alpers@ifm.uni-hamburg.de

(2) Hong Kong Observatory, 134A, Nathan Road, Kowloon, Hong Kong Emails: wkwong@hko.gov.hk, pwchan@hko.gov.hk,
(3) Nansen Environmental and Remote Sensing Center (NERSC), Thormøhlensgate 47, 5006 Bergen, Norway, Email: kfd@stormgeo.com

ABSTRACT

An atmospheric frontal system over the South China Sea (SCS) arising from the replenishment of the northeast monsoon is investigated by using multi-sensor satellite data, weather radar data, and a numerical model. The replenishment or freshening of the northeast monsoon results from the merging of high pressure areas over the Chinese Continent. The near-sea surface wind field associated with this event was measured by the Advanced Scatterometer (ASCAT) onboard the European MetOp satellite and the Advanced Synthetic Aperture Radar (ASAR) onboard the European Envisat satellite. The high resolution ASAR image reveals that the frontal line separating this wind field from the synoptic-scale ambient wind field is as sharp as in the case of a cold air outbreak and contains embedded rain cells. Furthermore, it shows that this replenishment was associated with northeasterly winds with speeds of up to 13 ms^{-1} over the SCS at offshore distances larger than 60 km, but only with speeds of around 6 ms^{-1} near the coast. The comparison of the observational data with model results of the pre-operational version of the AIR (Atmospheric Integrated Rapid-cycle) forecast model of the Hong Kong Observatory shows that the AIR model can successfully simulate the time evolution of the frontal system and the wind field over the open ocean, but fails to simulate the wind field near the coast.

1. INTRODUCTION

During the winter monsoon season in South East Asia high wind events often occur at the Chinese coast in the South China Sea (SCS). During these events, cold air from Siberia, Mongolia or northern China advances southward over the Chinese Continent, reaching the Chinese coast and advancing further over the SCS. Usually these events occur in the form of cold air outbreaks and are associated with a sudden freshening of the wind from a northerly direction and a sudden drop in air temperature. In Hong Kong, these events are also called cold or northerly winter monsoon surges. They occur most frequently between November and February, typically one to two times per month, and may last from a few days to one week or more [1], [2]. Northerly surges have been studied extensively using conventional meteorological data (see, e.g., [3]-[6]) and recently also by using satellite data, in particular high resolution synthetic aperture radar (SAR) data [7].

In this paper we report about another high wind event associated with the winter monsoon which is comparable with northerly surges in frequency of occurrence, and gives rise to similar sharp wind fronts over the SCS as northerly surges and to similar high wind speeds, but in this case from a northeasterly direction. However, the physical mechanism causing this frontal system over the SCS is different from the northerly surge. It is not associated with the advancement of a cold front, but with the replenishment of the northeast monsoon caused by to the merging of high pressure areas over the Chinese Continent. In this paper, such an event is studied for the first time using data from a suit of remote sensing instruments. The satellite data are from the scatterometer onboard the European MetOp satellite, called ASCAT (Advanced Scatterometer), the synthetic aperture radar (SAR) data onboard the European Envisat satellite, called ASAR (Advanced Synthetic Aperture Radar), the imaging multi-spectral radiometers (vis/IR) onboard the Japanese geostationary satellite MTSAT-1R, and the Special Sensor Microwave Imager (SSM/I) onboard the American DMSP F-15 satellite. Furthermore, we use data from the weather radar of the Hong Kong Observatory and meteorological data from weather stations and weather charts. These observational data are compared with model results of the pre-operational

Proc. of 'SEASAR 2012', Tromsø, Norway
18-22 June 2012 (ESA SP-709, March 2013)

version of the AIR (Atmospheric Integrated Rapid-cycle) forecast model of the Hong Kong Observatory [8] and it is shown that this model reproduces quite well the observational data over the open ocean, but not close to the coast. Thus, with this paper, for the first time, the AIR model has been subject to a test of its ability to simulate frontal systems over the SCS caused by the replenishment of the northeast monsoon. Furthermore, the comparison of observational data with model results provides valuable input for improving the AIR model. A better forecast of high wind speed events over the SCS associated with the northeast monsoon is of great relevance to marine operations, e.g., at oil drilling platforms.

2. THE METEOROLOGICAL SITUATION

The weather chart at mean sea level pressure (MSLP) at 0000 UTC on 28, 29, 30, and 31 December 2009 are depicted in Figs. 1 - 4. The weather chart of 28 December (Fig. 1) shows a high pressure area residing over southeastern China centered at Nanchang (Jiangxi Province), maintaining a northeast monsoon over southern China and the northern part of the South China Sea. This is characterized by the narrow spacing of the isobars over the region implying a high pressure gradient. On 29 December 2010, the northeast monsoon

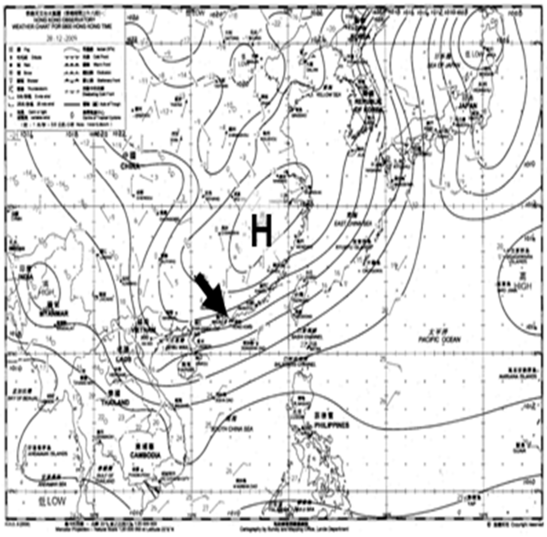

Figure 1. Weather chart (at mean sea level) of South East Asia valid for 0000 UTC on 28 December 2009 showing a high pressure area residing over southeastern China northeast of Hong Hong giving rise to northeasterly winds over southern China and the northern part of the South China Sea. The arrow points to the location of Hong Kong.

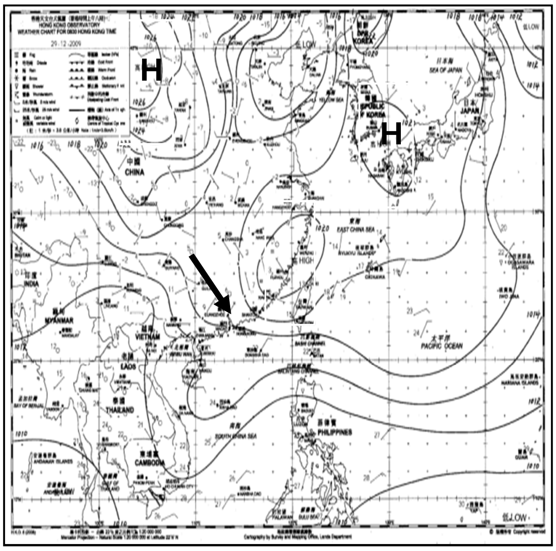

Figure 2. Same as Fig. 1, but valid for 0000 UTC on 29 December 2009 showing that the high pressure center over southern China has moved further south causing a turn of the wind to the east in the Hong Kong area. Furthermore, it shows another high pressure center over northern China.

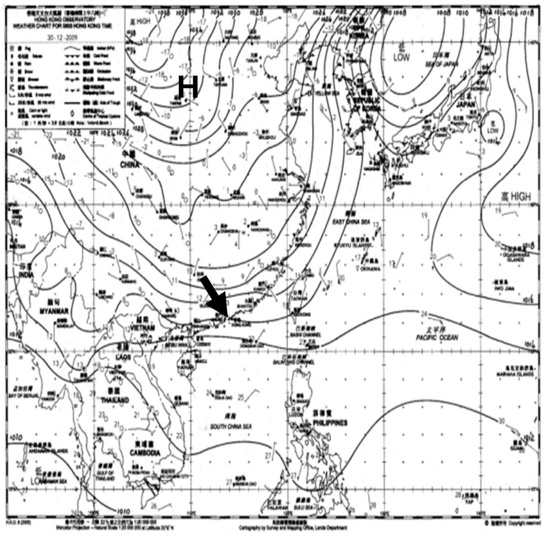

Figure 3. Same as Fig. 1, but valid for 0000 UTC on 30 December 2009 showing that the high pressure areas over eastern China and the southern Sea of Japan have merged with the high pressure area over northern China leading to a replenishment of the northeast monsoon. The high pressure gradient characterized by the dense spacing of the isobars and associated with the wind front is located north of Hong Kong.

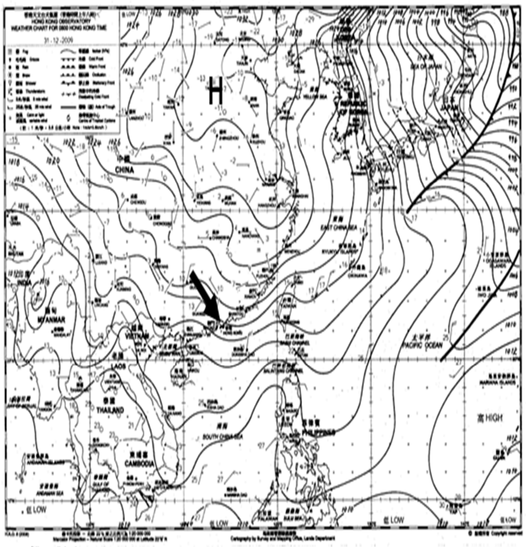

Fiure. 4. Same as Fig. 1, but valid for 0000 UTC on 31 December 2009 showing that the replenishment of the northeast monsoon has reached the northern part of the South China Sea

has slackened, which is characterized by the wider spacing of the isobars over southern China and the northern part of the SCS (Fig. 2). Between these two dates, the center of the high pressure area had moved southward resulting in a turn of the wind from E to NE over southern China. Note that on this day, another high pressure area has emerged over northern China. On 30 December the high pressure areas over eastern China and the southern Sea of Japan merged with the high pressure area over northern China leading to a replenishment of the northeast monsoon (Figure 3). At 0000 UTC on 30 December (Fig. 3) the high pressure gradient (narrow spacing of the isobars) was lying over the Chinese continent, while at 0000 UTC on 31 December (Fig. 4) it was lying over the northern part of the SCS. Thus it must have crossed the southern Chinese coast near Hong Kong between these two dates causing an increase of the wind speed and a turn of the wind direction

We infer from the weather charts that the cold air, before reaching the sea area south of Hong Kong, had travelled along the east coast of China through the Strait of Taiwan and warmed by the sea. The water temperature near Hong Kong was at that time around 22ºC and the air temperature 16ºC. This air temperature was measured at Waglan Island located 6 km southeast of Hong Kong (22°10'56" N; 114°18'12" E) at 0200 UTC on 30 December, i.e., approximately at the time the SAR data acquisition. The arrival of the cooler continental undercut the warmer air over the sea causing convection. This caused an increased transport of vertical momentum from the marine boundary layer top to the sea surface and thus an increase in near-sea surface wind speed.

3. REMOTE SENSING DATA

3.1. ASCAT DATA

Figs. 5 and 6 show near-surface wind fields measured by ASCAT onboard the European MetOp satellite at 1358 UTC (2158 Hong Kong Time (HKT)) on 29 December 2009 and at 0226 UTC (1026 HKT) on 30 December 2009, respectively. The near-surface wind speed is measured by this instrument indirectly via the small-scale sea surface roughness. ASCAT measures the near-surface wind field on both sides of the satellite track along two swathes that have widths of approximately 500 km. It has totally six antennas, three looking to each side of the satellite track. The spatial resolution is 25 km, and the data are digitized at a spacing of 12.5 km. (http://www.esa.int/export/esaME/ascat.html). The wind fields retrieved from ASCAT data, and also from ASAR data, are referenced to a height of 10 m above the sea surface and to neutrally stable atmosphere. Fig. 5 shows a distinct high wind speed band adjacent to the coast with winds blowing from a northeasterly direction and wind speeds between 8 and 11 ms^{-1} (greenish colors). Note that, due to the coarse resolution of 25 km, ASCAT cannot measure the wind field close to the coast, because at distances smaller than 25 km the resolution cell would contain land targets and thus contaminate the radar

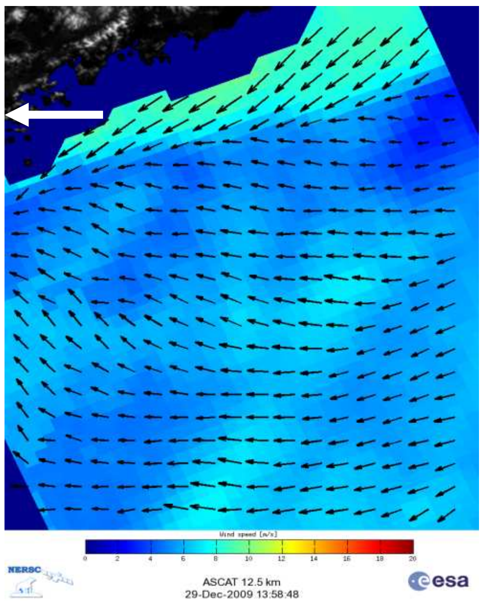

Figure 5. Near-surface wind field retrieved from data of the ASCAT scatterometer onboard the MetOp satellite at 1358 UTC (2158 HKT) on 29 December 2009. The arrow points to the location of Hong Kong, © ESA

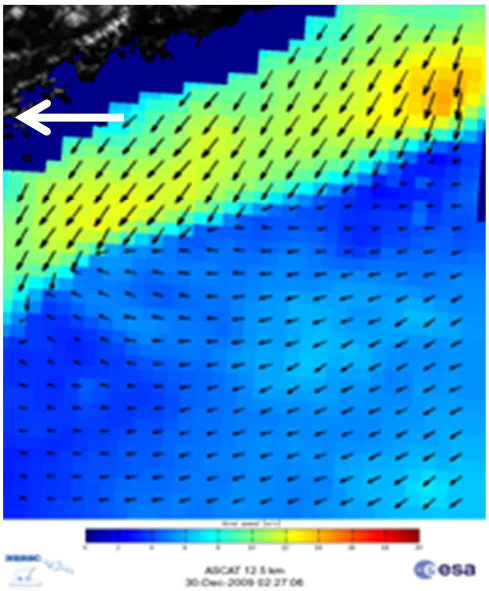

Figure 6. Same as Fig. 5, but at 0227 UTC (1027 HKT) on 30 December 2009. © ESA

backscattering signal. Fig. 6 shows that 12 hours and 28 minutes later (at 0226 UTC on 30 December 2009) the frontal line has moved further south. At this time, the wind speed in the coastal band has increased to a maximum of about 14 ms^{-1} (brownish colors).

3.2. ASAR DATA

Fig. 7 shows an ASAR image of the sea area south of Hong Kong which was acquired only 13 minutes earlier (at 0213 UTC) than the ASCAT data shown in Fig. 6. This ASAR image was acquired at VV polarization in the Wide Swath (WS) Mode, with a swath width of 400 km and a spatial resolution of 150 km. Visible are in the upper left hand corner the Chinese coast with Hong Kong, marked by an arrow, and in the central left hand section the coral reef of Dongsha island (black circle). Almost parallel to the coast line, a broad band of increased image brightness is visible which is caused by increased sea surface roughness and thus by increased near-surface wind speed. Noteworthy is the very sharp southern boundary of this high roughness band, which marks the frontal line. Its offshore distance near Hong Kong is approximately 110 km and increases towards east to more than 150 km. Elongated dark patches are visible in the eastern section of the image adjacent to the frontal line (on the southern side). We interpret them as radar signatures of surface films, probably caused by mineral oil released from ships or oil platforms. They dampen the short surface waves and thus reduce the

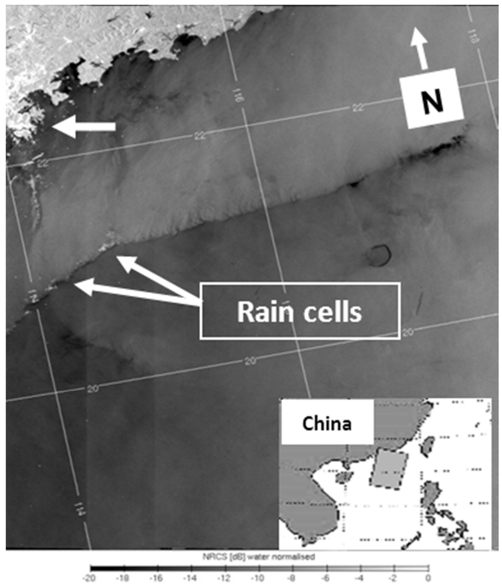

Figure 7. SAR image acquired by Envisat ASAR in the Wide Swath mode (VV polarization) at 0213 UTC (1013 HKT) on 30 December 2009 over the Chinese coast of the South China Sea near Hong Kong. The imaged area is 510 km x 660 km. The inset shows the location of the SAR scene in the South China Sea. The arrow points to the location of Hong Kong. © ESA

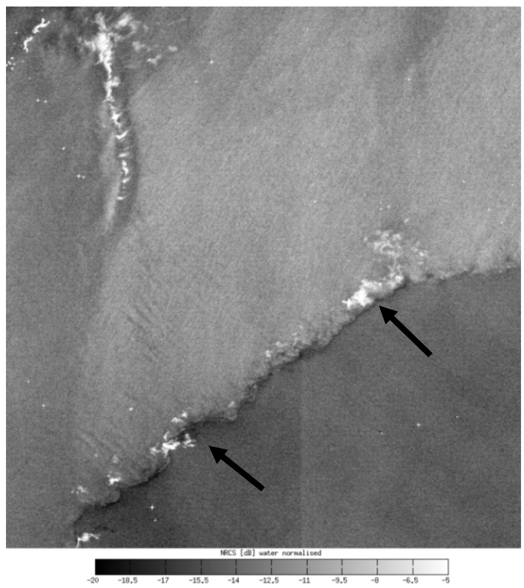

Fiure 8. Zoom-in view on the central western section of the SAR image depicted in Fig. 7 showing details of the frontal line. The white patches are radar signatures of rain cells.

radar backscattering [9], which makes them to appear dark on radar images. The bright spots embedded in the frontal line, as well as the bright line north of these bright spots, are radar signatures of rain cells. The sea area showing rain cells is shown in greater detail in Fig. 8. The bright spots visible on the image are caused by rain. Evidence of this interpretation is provided by the quasi-simultaneously acquired weather radar image depicted in Fig. 10. Noteworthy is that the rain cells are located in the wind front. We interpret this as being caused by the frontal circulation transporting moist air at the converging zone to the lifted condensation level. This is in agreement with high-resolution water vapor data retrieved from SAR data of the European satellites ERS-1 and ERS-2 flying in a tandem mission [10]. Fig. 9 shows the near-surface wind field retrieved from this ASAR image. Note, that due to its finer resolution, ASAR can measure the near-surface wind field much closer to the coast than ASCAT. Here the wind field shown has been processed to a resolution of 1 km x 1 km for a more accurate estimate of the wind speed.

The retrieval of near-surface wind fields from SAR data is not as straightforward as from scatterometer data [11]. While scatterometers measure the backscattered radar power from a resolution cell on the sea surface from (at least) three different azimuth directions, SARs measure it only from one direction, perpendicular to the satellite flight direction. Thus, in order to retrieve (two-dimensional) wind fields from SAR images, one has to get the wind direction from other sources than from backscattered radar power values [12]-[14]. This directional information can be obtained from 1) atmospheric models, 2) linear features visible on the SAR images, which are assumed to be aligned in wind direction, or from 3) sensors measuring the wind direction. In our case, we have taken the wind direction from ASCAT data acquired only 13 minutes after the ASAR image, see Fig. 6. Close to the coast, where ASCAT has no coverage due to land contamination of the signal, we have supplemented it with directions from the NCEP GFS atmospheric model. NCEP GFS is the abbreviation for Global Forecast System (GFS) model developed by the National Centers for Environmental Prediction (NCEP). It provides global wind fields every three hours at a grid spacing of 0.5° in latitude and longitude. Here we have taken the data valid for 0300 UTC, i.e., 47 minutes after the ASAR data acquisition.

For the inversion of the radar backscattering values into wind speed, we have used the “C-band Wind Scatterometer MODel Function version 4” (CMOD4) [11], which originally was developed to retrieve near-surface wind fields from data of the wind scatterometer onboard the European ERS-1 and ERS-2 satellites. Fig. 9 shows that the strongest winds were encountered at off-shore distances between 60 and 100 km, and the lowest

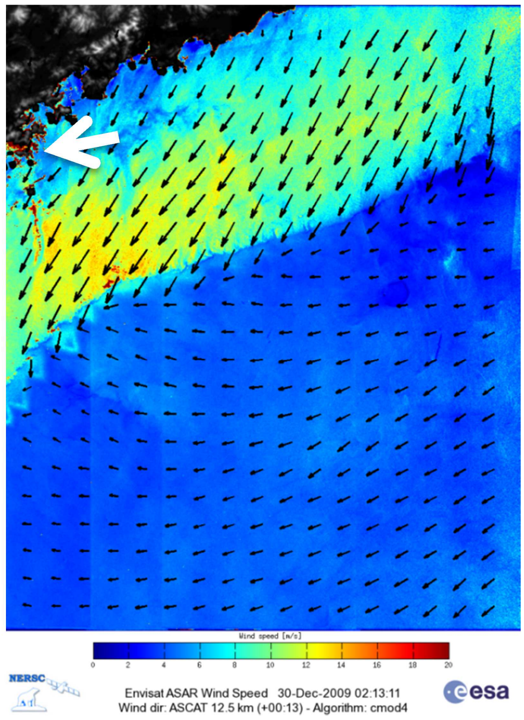

Figure 9. Near-surface wind field retrieved from the SAR image by using the wind direction measured by ASCAT 13 minutes after ASAR data acquisition (see Fig. 6) and, near the coast, provided by the NCEP model. The arrow points to the location of Hong Kong.

winds und near the coast. We attribute the low wind speeds near the coast to wind shadowing caused by elevated coastal topography east of Hong Kong.

3.3. WEATHER RADAR AND MTSATT-1R CLOUD IMAGES

Fig. 10 shows the distribution of rain observed by the Hong Kong weather radar at 0212 UTC (1012 HKT) on 30 December 2009, one minute before the SAR data acquisition. Note the two distinct strong rain cells in the rain band which are marked by arrows. Their positions closely correspond to the positions of the two distinct bright patches visible on the ASAR image marked in Fig. 8 by arrows. Fig. 11 shows a cloud image which was acquired in the visible channel by the Japanese geostationary satellite MTSAT-1R over the SCS and the Chinese Continent at 0157 UTC on 30 December 2009, i.e., 16 minutes before the SAR data acquisition. The resolution of the MTSAT-1R images is at nadir 1 km. It shows clouds along the Chinese coast which have a sharp southern boundary. In particular, a narrow band of enhanced cloud density is visible south of Hong Kong (marked by an arrow). This is the area of strong convection which is prone to the development of rain cells.

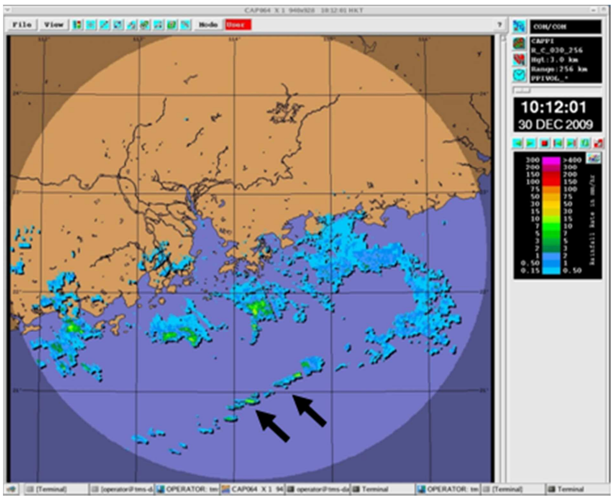

Figure 10. Radar reflectivity image acquired by the Hong Kong weather radar at 0212 UTC (1012 HKT) on 30 December 2009 converted into rainfall showing the distribution of rain around Hong Kong. Note that the position of the rain band coincides with the fontal line visible on the ASAR image depicted in Figs. 7 and 8.

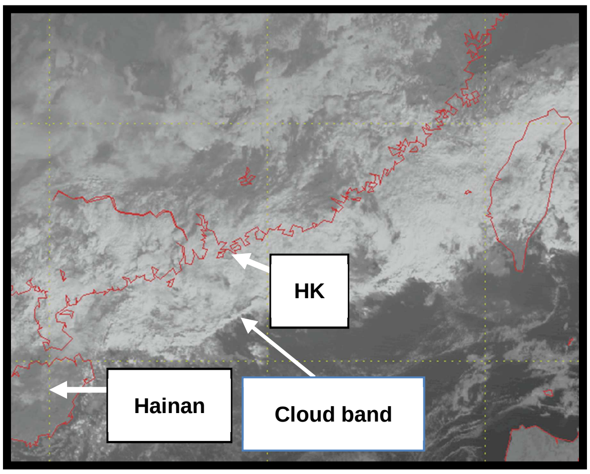

Figure 11. Cloud image acquired in the visible band by the Japanese geostationary satellite MTSAT-1R at 0157 UTC (0957 HKT) on 30 December 2009 over the South China Sea and the Chinese Continent. The narrow band of enhanced cloud density at the southern boundary of the cloud field coincides with the wind front visible on the wind maps depicted in Figs. 6 and 9. © JAX.

3.4. SSSM/I CLOUD LIQUID WATER CONTENT DATA

Fig. 12 shows two maps of cloud liquid water content derived from data acquired in the microwave band by the Special Sensor Microwave Imager (SSM/I) onboard the American Defense Meteorological Satellite Program *(DMSP) satellite F-15 (launched 2008) (www.ssmi.com).* The maps were acquired at 2248 UTC on 29 December (3 hours and 25 minutes before the SAR data) and at 2224 UTC on 30 December (20 hours and 9 minutes after the SAR data), respectively. The resolution is 45 km (http://www.osdpd.noaa.gov/ml/air/clouds.html). The frontal line is also clearly visible on these maps. These images reveal higher cloud liquid water content to the north of the frontal line, in agreement with the observed rain areas visible on the weather radar images.

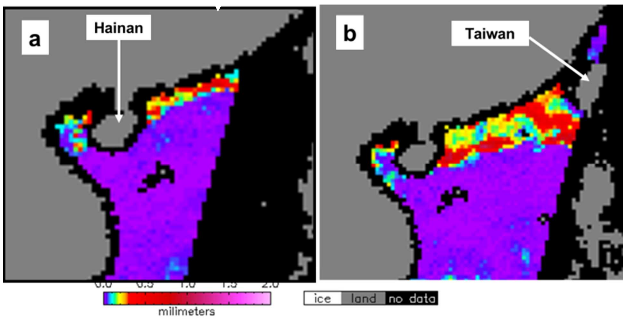

Figure 12. Cloud liquid water content inferred from SSM/I data acquired at (a) 2248 UTC 29 December 2009 (left plot) and (b) 2224 UTC 30 December 2009 (right plot) showing the propagation of the frontal line southeastwards.

4. COMPARISON OF REMOTE SENSING DATA WITH MODEL FORECAST

Figs. 13 and 14 show simulations carried out with the AIR model with a resolution of 10 km. They show the near-surface wind (10 m level) and air temperature (2 m level) calculated by the AIR model for 1400 UTC on 29 December and for 0200 UTC on 30 December 2009, respectively. The air temperature is shown by the color coding and the wind vector by conventional wind barbs (plotted here with a lower resolution)**.** Fig. 13 shows that cold air is flowing through the Strait of Taiwan in a southwestward direction and encounters west of this strait the ambient synoptic wind which blows from an easterly direction. A frontal line of flow convergence is generated which coincides with the temperature front. Here moist air is lifted upward with the potential to generate rain cells. Fig. 14 shows that at 0200 UTC on

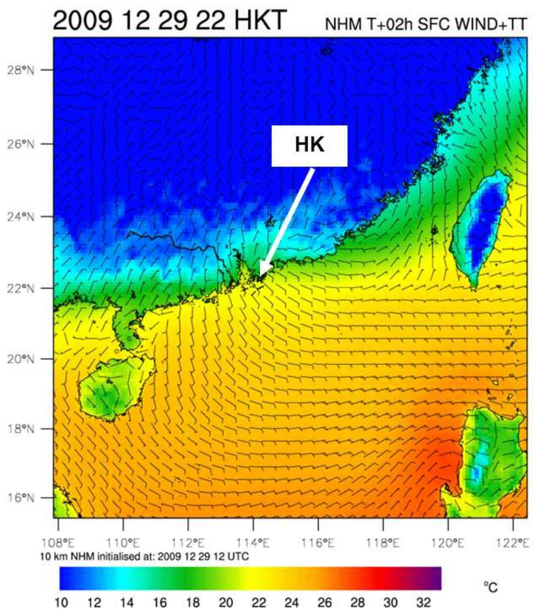

Figure *13. Near-surface wind (10 m level) wind and air tgemperature (2 m level) calculated by the AIR model with 10 km resolution for 1400 UTC on 29 December 2009 The air temperature is shown by the color coding and the wind vector by conventional wind barbs.*

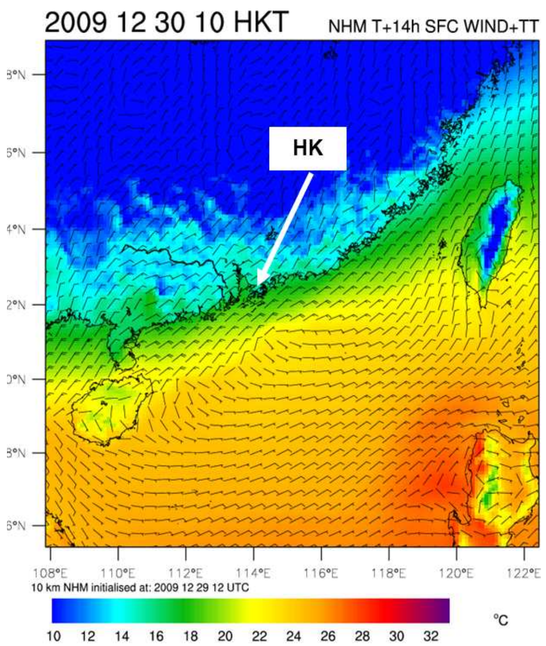

Figure 14. Same as Fig. 15, but for 0200 UTC on 30 December 2009. The air temperature is shown by the color coding and the wind vector by conventional wind barbs.

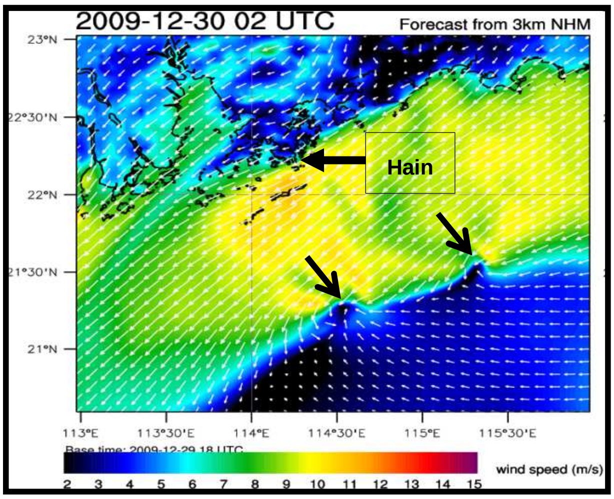

Figure 15. Near-surface wind vectors (white arrows) and wind speed (color coding) calculated by the AIR model with 3 km resolution for 0200 UTC (1000 HKT) on 30 December 2009.

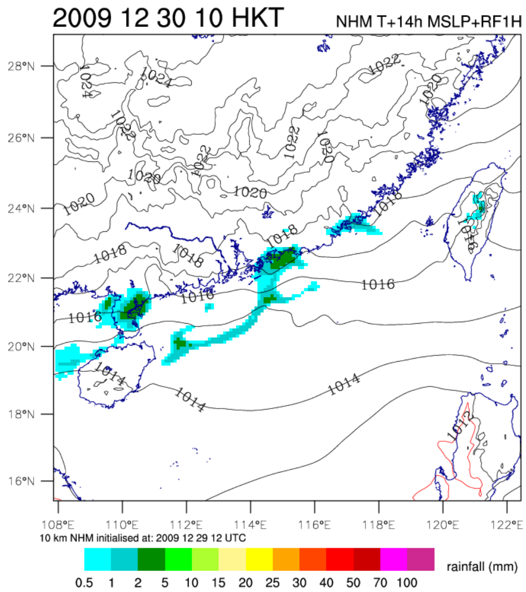

Figure 16. Mean-sea-level pressure (contours) and 1-hour accumulated rainfall (color shading) calculated by the AIR model with 10 km resolution for 0200 UTC (1000 HKT) 30 December 2009.

30 September, i.e., 13 minutes before the SAR data acquisition (Fig. 7), the cold air has advanced further west (beyond t*he* Chinese island Hainan) and is accompanied by a wind front extending along the southern Chinese coast.

Fig. 15 shows the simulations of the near-surface wind field (10 m level) with a resolution of 3 km for 0200 UTC on 30 December 2009. In contrast to Figs. 13 and 14, here the color coding denotes wind speed, and the arrows denote again wind direction. The simulated wind fields depicted in Figs. 14 and 15 resemble closely the ones measured by ASAR and ACAT at 0213 and 0227 UTC, respectively. In the simulations the wind is blowing from NE and has a variable speed between 6 and 11 ms^{-1} which is slightly lower than the wind fields derived from the ASCAT (Fig. 6) and ASAR data (Fig. 9), which shows wind speeds of up to 13 ms^{-1}. However, there is one significant difference between the SAR-derived and the simulated wind fields. While the SAR-derived wind field shows low wind speeds in the coastal area east of Hong Kong (around 4 ms^{-1}), the simulations show in this area much higher wind speeds (between 8 and 10 ms^{-1}). The lower wind speed in this area is in agreement with the wind measurements made at the meteorological station on Waglan Island, where at 0200 UTC on 30 December a wind speed of 7.5 ms^{-1} was measured. We attribute this lower wind speed to shadowing of the northeasterly wind by the coastal topography east of Hong Kong, which apparently is not taken into account properly in the AIR model. However, farther away from the coast, this event was associated with much higher wind speeds (up to 13 ms^{-1}).

Note the two kinks in the frontal line marked by arrows. They seem to be areas prone to develop rain cells (see Fig.10).

Fig. 16 shows the distribution of 1-hour accumulated rainfall at 0200 UTC on 30 December calculated by the AIR model with a resolution of 10 km. It shows a rain band which makes landfall just east of Hong Kong. This is in agreement with the weather radar image depicted in Fig. 10. But due to the limited coverage of the weather radar, no further comparisons can be made. However, an interesting observation is that the simulations show that the rain band terminates east of Hainan, which is in agreement with the cloud image depicted in Fig.11 which shows no clouds in this area**.**

5. SUMMARY AND CONCLUSIONS

For the first time, a coastal wind front over the South China Sea associated with the replenishment of the northeast monsoon has been investigated using multi-sensor satellite data, weather radar data, and a meso-scale atmospheric model. The replenishment of the northeast monsoon was caused by the merging of high pressure areas over northern China and the southeast of China. This gave rise to a wind front spreading southward over the SCS. The replenishment of the northeast monsoon gave rise to a strengthening of northeasterly wind with speeds of up to 13 ms^{-1} over the SCS . However, close to Hong Kong, the SAR-derived wind field only shows winds up to 6 ms^{-1} which is not in agreement with model calculations, but confirmed by wind measurements made at Waglan Island which is located 6 km southeast of Hong Kong. We attribute this to shadowing of the northeasterly wind by the coastal topography east of Hong Kong, which apparently is not taken into account properly in the AIR model.

High wind speed events at the southeast coast of the SCS are often caused by cold air outbreaks, also called northerly surges. They are associated with a sudden increase if wind speed from a northerly direction and a large drop in air temperature at Hong Kong. But the high wind speed event investigated in this paper was of a different kind. At Hong Kong, it was associated only with a small drop in air temperature and a very small change in wind speed and direction. The reason for the small drop in air temperature is that the originally cold air had travelled along the Chinese coast over warm waters and thus had been warmed considerably High winds with speeds up to 13 ms^{-1} blowing from NE were only encountered far offshore (beyond 60 km), but not close to the coast. Furthermore, the wind front which it formed with the ambient easterly wind is similarly sharp (with widths around 2 km) as in the case of a northerly surge [7] and has embedded rain cells.

By comparing time series of MTSAT-IR cloud images with weather radar images, we have observed that, at the early stage of the frontal development of the frontal system, the southward motion of the cloud front was closely related to the motion of the rain band. However, at later stages, the southward motion of the rain band partially decoupled from the motion of the cloud line leading to a fall back of the rain band behind the cloud line.

ACKNOWLEDGMENT

We thank ESA for providing the ASAR images free of charge within the ESA-MOST Dragon 2 project, and Gerd Müller of the Meteorological Institute of the University of Hamburg for very fruitful discussions on the interpretation of the observed atmospheric phenomena.

REFERENCES

1 Wu, M.C. & Chan, J.C.L. (1997). Surface features of winter monsoon surges over South China.. *Mon. Wea. Rev.,* **125**, 317–340.

2 Zhang, Y., Sperber, K.R. & Boyle, J.S. (1997). Climatology and interannual variation of the East Asian winter monsoon: Results from the 1979–95 NCEP–NCAR reanalysis. *Mon. Wea. Rev*. **125**, 2605–2619.

3 Lim, H. & and Chang, C/.-.P. (1981). A theory for midlatitude forcing of tropical motions during winter monsoon. *J. Atmos. Sci*., **38**, 2377–2392.

4 Chu, P.-S. & Park, S.-U. (1984). Regional circulation characteristics associated with a cold surge event over East Asia during Winter MONEX. *Mon. Wea. Rev*., **112**, 955–965.

5 Johnson, R.H. & Zimmerman, J.R. (1986). Modification of the boundary layer over the South China Sea during a Winter MONEX cold surge event. *Mon. Wea. Rev*., **114**:2004–2015.

6 Chen, T.C., Huang, W.R. & Yoon, J. (2004). Interannual variation of the East Asian cold surge activity. *Journal of Climate,* **17:2**, 401-413.

7 Alpers, W., Wong, W.K., Dagestad, K.-F. & Chan, P.W. (2012). A northerly winter monsoon surge over the South China Sea studied by remote sensing and a numerical model. *Int. J. Rem. Sens*. **33:23**, 7361-7381.

8 Wong, W.K. (2010). Development of an Operational Rapid Update Non-hydrostatic NWP and Data Assimilation Systems in the Hong Kong Observatory. The 3th International Workshop on Prevention and Mitigation of Meteorological Disasters in Southeast Asia, 1-4 March 2010, Beppu, Japan.

9 Valenzuela, G.R. (1978). Theories for the interaction of electromagnetic and oceanic waves: A review, *Boundary.-Layer Meteor*. **13**, 61-85.

10 Hanssen, R.F.I., Weckwerth,T.M., Zebker, H.A. & Klees, R. (1999). High-resolution water vapor mapping from interferometric radar measurements. *Science* **283**, 1297 -1299.

11 Stoffelen, A. & Anderson, D. (1997). Scatterometer data interpretation: Estimation and validation of the transfer function CMOD4. *J. Geophys. Res.* **102** (C3), 5767–5780.

12 Horstmann, J. & Koch, W. (2005). Comparison of SAR wind field retrieval algorithms to a numerical model utilizing ENVISAT ASAR data. *IEEE J. Oceanic Eng.* **30**, 508–515.

13 Sikora, T.D., Young, G.S, & Winstead, T.S. (2006). A novel approach to marine wind speed assessment using synthetic aperture radar, *Wea. Forecasting*, **21**, 109-115.

14 Alpers, W., Ivanov, A.Yu. & Dagestad, K.-F. (2011). Encounter of foehn wind with an atmospheric eddy over the Black Sea as observed by the synthetic aperture radar onboard Envisat. *Mon. Wea. Rev*. **139**, 3992-4000.